Title
A first search for cosmogenic neutrinos with the ARIANNA Hexagonal Radio Array

Authors
Barwick, SW
Berg, EC
Besson, DZ
et al.

Publication Date
2015-10-01

DOI
10.1016/j.astropartphys.2015.04.002

Peer reviewed

A First Search for Cosmogenic Neutrinos with the ARIANNA Hexagonal Radio Array

S.W.Barwick[a], E.C.Berg[a], D.Z.Besson[c,g], G.Binder[e,f], W.R.Binns[m], D.Boersma[j], R.G.Bose[m], D.L.Braun[m], J.H.Buckley[m], V.Bugaev[m], S.Buitink[k], K.Dookayka[a], P.F.Dowkontt[m], T.Duffin[a], S.Euler[j], L.Gerhardt[e], L.Gustafsson[j], A.Hallgren[j], J.C.Hanson[c,a], M.H.Israel[m], J.Kiryluk[i], S.Klein[e,f], S.Kleinfelder[b], H.Niederhausen[i], M.A.Olevitch[m], C.Persichelli[a], K.Ratzlaff[d], B.F.Rauch[m], C.Reed[a,*], M.Roumi[b], A.Samanta[b], G.E.Simburger[m], T.Stezelberger[e], J.Tatar[a,h,*], U.Uggerhoj[l], J.Walker[a], G.Yodh[a], R.Young[d],

(The ARIANNA Collaboration)

[a]*Dept. of Physics and Astronomy, University of California, Irvine, USA*
[b]*Dept. of Electrical Engineering and Computer Science, University of California, Irvine, USA*
[c]*Dept. of Physics and Astronomy, University of Kansas, USA*
[d]*Instrumentation Design Lab, University of Kansas, USA*
[e]*Lawrence Berkeley National Laboratory, USA*
[f]*Dept. of Physics, University of California, Berkeley, USA*
[g]*Moscow Engineering and Physics Institute, Russia*
[h]*Center for Experimental Nuclear Physics and Astrophysics, University of Washington, USA*
[i]*Stonybrook University, USA*
[j]*University of Uppsala, Sweden*
[k]*University of Nijmegen, The Netherlands*
[l]*Aarhus University, Denmark*
[m]*Dept. of Physics and McDonnell Center for the Space Sciences, Washington University, St. Louis, USA*

Abstract

The ARIANNA experiment seeks to observe the diffuse flux of neutrinos in the $10^8 - 10^{10}$ GeV energy range using a grid of radio detectors at the surface of the Ross Ice Shelf of Antarctica. The detector measures the coherent Cherenkov radiation produced at radio frequencies, from about 100 MHz to 1 GHz, by charged particle showers generated by neutrino interactions in the ice. The ARIANNA Hexagonal Radio Array (HRA) is being constructed as a prototype for the full array. During the 2013-14 austral summer, three HRA stations collected radio data which was wirelessly transmitted off site in nearly real-time. The performance of these stations is described and a simple analysis to search for neutrino signals is presented. The analysis employs a set of three cuts that reject background triggers while preserving 90% of simulated cosmogenic neutrino triggers. No neutrino candidates are found in the data and a model-independent 90% confidence level Neyman upper limit is placed on the all flavor $\nu + \bar{\nu}$ flux in a sliding decade-wide energy bin. The limit reaches a minimum of $1.9{\times}10^{-23}$ GeV^{-1} cm^{-2} s^{-1} sr^{-1} in the $10^{8.5} - 10^{9.5}$ GeV energy bin. Simulations of the performance of the full detector are also described. The sensitivity of the full ARIANNA experiment is presented and compared with current neutrino flux models.

Keywords: ARIANNA, Antarctica, ice, neutrino, cosmogenic, GZK, flux, high energy

1. Introduction

While the flux of cosmic rays has been measured to energies greater than 10^{10} GeV [1], the sources of such high energy particles remain a mystery. No known galactic source could accelerate particles to such energies, and no particular sources of the very highest energy particles, with large rigidities, have been found [2–5]. Potential sources of such ultra-high energy (UHE) cosmic rays are limited to our local supercluster (within about 50 Mpc) due to

*Corresponding author
Email addresses: cjreed@uci.edu (C.Reed), jtatar@uci.edu (J.Tatar)

their interaction with the cosmic microwave background (CMB) [6, 7]. The mesons produced by this process promptly decay to leptons, leading to a flux of UHE neutrinos [8–10].

Cosmogenic neutrinos may reveal cosmic accelerators beyond our local supercluster, as the mean free path of neutrinos through the CMB is larger than the visible universe. Such neutrinos would be produced within about 50 Mpc of the cosmic ray sources and would travel to Earth without deflection by magnetic fields, potentially pointing back to the accelerating objects.

Several large projects (AMANDA [11], IceCube [12, 13], ANITA [14–16] and RICE [17, 18]) exploit the fact that ice is transparent to Cherenkov radiation (at both optical and radio wavelengths) in order to search for cosmogenic neutrinos. These experiments complement cosmogenic neutrino searches by air shower detectors such as the Pierre Auger Observatory [19, 20] and HiRes [21, 22]. Below energies of 10^{10} GeV, IceCube currently provides the best constraints on the UHE neutrino flux and in the $10^4 - 10^6$ GeV range, IceCube has observed an extra-terrestrial diffuse neutrino flux [23].

A new generation of neutrino experiments is emerging with the efforts of ARA [24, 25], GNO [26] and the Antarctic Ross Ice Shelf Antenna Neutrino Array (ARIANNA, described in this paper). These experiments seek to extend the neutrino flux measurements to ultra-high energies by constructing radio Cherenkov detectors that are orders of magnitude larger in effective sensitive volume than current experiments using well-understood and inexpensive technology. Preparation is underway for the next generation of ballon-borne experiments as well [27], with efforts like that of EVA [28]. A large number of models predict cosmogenic neutrino fluxes that are measurable by such experiments with improved sensitivity to neutrinos above 10^8 GeV, particularly in the $10^8 - 10^{10}$ GeV range. See Sect. 2.2 for examples of such models.

The ARIANNA and ARA experiments are proposing the construction of arrays of radio detectors in Antarctica that will reach effective volumes $\mathcal{O}(100)$ km^3. A third radio experiment, GNO, is exploring the construction of a radio neutrino telescope in Greenland. These experiments will measure the radio-frequency (RF) pulse emitted by the charged particle shower resulting from a UHE neutrino interaction in ice via the Askaryan effect [29, 30]. The Askaryan radio pulse has been measured in a variety of dielectric materials using particle accelerators to induce charged particle showers [31, 32].

The ARIANNA collaboration plans to construct a 36×36 km^2 array of 1296 independent, autonomous radio detector stations just below the surface of the Ross Ice Shelf. The ice to water interface below the Ross Ice Shelf serves as a mirror for radio waves, allowing the stations to observe neutrinos arriving from the sky above the detector as well as from the horizon. The detector will measure radio frequencies between about 100 MHz $-$ 1 GHz. This bandwidth is sensitive to the linear increase in power of the Askaryan pulse with frequency up to $\sim$1 GHz for signals measured on the Cherenkov cone [33].

The ARIANNA site is roughly 100 km from the McMurdo Antarctic Station, which provides logistical support during construction. Despite the relative closeness of McMurdo, the ARIANNA site is free of anthropogenic RF noise due to its being buffered by Minna Bluff to the north and the Transantarctic Mountains to the west.

Properties of the ice at the ARIANNA site have been measured by transmitting polarized radio pulses into the ice and observing the reflected pulses at multiple locations. These measurements indicate that the ice to water interface is a near perfect mirror. The attenuation length, measured to be between 400 and 500 m for radio frequencies, is found to be comparable to the average thickness of the Ross Ice Shelf. The ice shelf thickness has been measured to be 576 ± 8 m [34] including a firn layer within the upper 60-70 m [35] (approximately). The firn layer is characterized by a monotonic increase in mass density as a function of depth. A more complete discussion of the ice properties at the ARIANNA site is presented in Ref. [34].

The construction of the ARIANNA Hexagonal Radio Array (HRA) is approved for completion during the 2014-2015 austral summer. This array of seven ARIANNA stations serves as a research and development project for the full ARIANNA array [36]. Each HRA station consists of four log-periodic dipole antennas (LPDAs), a high-speed data acquisition (DAQ) system, wireless communication peripherals and local renewable power generation.

The expected performance of the full ARIANNA telescope is presented in Section 2. The performance of the HRA stations is discussed in Section 3. A first search for neutrino signals in the HRA data is described in Section 4.

2. The ARIANNA Telescope

The ARIANNA experiment plans to measure the cosmogenic neutrino flux using a large surface array of radio receivers. ARIANNA will build upon previous UHE neutrino searches by greatly increasing the size of the detector. This will improve the sensitivity to neutrinos of $10^8 - 10^{10}$ GeV by a factor of 13 or more, depending on model, relative to the current best limits (see Sect. 2.2.2). In order to maximize the effective volume of the telescope, each ARIANNA station of the 36×36 array will be separated from neighboring stations by 1 km, so that a typical neutrino pulse will be observed by a single station. The stations will measure the amplitude and direction of the incoming radio pulse using multiple antennas, allowing the energy and source direction of the primary neutrino to be determined.

The ice to water interface at the bottom of the Ross Ice Shelf provides a near perfect mirror for radio waves [34]. This allows the surface detectors to measure reflected radio pulses produced by downgoing neutrino-induced showers, in addition to directly measuring the Askaryan radiation of horizontal showers. As the Earth is opaque to UHE neutrinos, this (greater than) 2π sr solid angle acceptance contributes heavily to the high sensitivity of the ARIANNA telescope. The sensitivity of the experiment also benefits from a low energy threshold (below 10^8 GeV) and from the large number of detector stations made possible by the ease of installation at the ice surface.

The flagship measurement of the ARIANNA telescope will be the observation of the flux of cosmogenic neutrinos in the $10^8 - 10^{10}$ GeV range. The predicted flux of these neutrinos depends on the chemical composition of UHE cosmic rays, the cosmic ray injection spectrum and the cosmic ray source evolution [37]. A measurement of the neutrino flux will provide additional input to help constrain these parameters and thus improve the understanding of both neutrino and cosmic ray sources.

The observation of a significant number of neutrinos by ARIANNA would allow further measurements to be performed. The shape of the neutrino energy spectrum can help distinguish a flux due to strong source evolution from one due to a soft injection spectrum [38, 39]. A search for point-like sources of UHE neutrinos will be a primary goal and has the potential to reveal particle accelerators at distances beyond our local supercluster. Further, the neutrino-nucleon cross section can be measured at center of mass energies around 10 TeV through the angular dependence of the flux [40, 41]. In addition, the flavor composition of the neutrino flux may be explored [42]. Once the flux of neutrinos is known, such observations may be improved by redeploying the surface detectors in order to maximize angular and energy resolution.

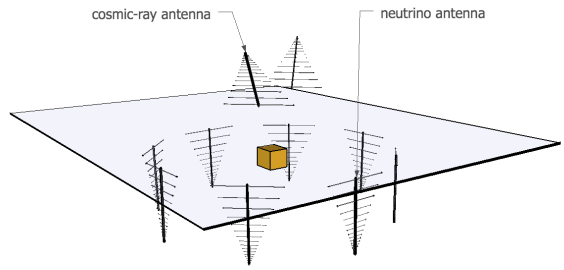

Figure 1: An illustration of the antenna arrangement in a single ARIANNA station. For simulations of cosmic ray showers, all ten antennas are included in the simulation. For simulations of the detector response to neutrino signals, only the eight downward facing antennas are simulated. The stations built for the HRA detector use a smaller subset of only four downward facing antennas, arranged in a square.

Even the lack of a measurable neutrino flux would have profound consequences. Such a scenario would imply that either the sources of the highest energy cosmic rays are local, or that the sources have astrophysically interesting properties, such as an iron-dominated composition with a hard energy injection spectrum and an acceleration energy cutoff below the photo-fragmentation threshold [43].

The expected performance of the full ARIANNA experiment, described in Sect. 2.2, is determined through the simulation of stations with eight downward facing LPDAs, as shown in Fig. 1. Studies of cosmic ray air showers suggest that ARIANNA may trigger on radio pulses from such events. To that end, the addition of two antennas that are directed upward at a 45° angle has been studied, as presented in Sect. 2.3.

2.1. Simulation Methods

The performance of the ARIANNA telescope, detailed in Sect. 2.2, has been characterized by simulating the production and detection of radio signals in the frequency domain. An additional simulation package, presented in Sect. 2.1.2, has been developed to study the response of the detector in the time domain. The analysis of HRA data, discussed in Sect. 4, combines both simulation tools in order to estimate expected neutrino signals.

2.1.1. Frequency Domain

A set of simulation tools has been developed and used to calculate the sensitivity and model the performance of the ARIANNA telescope. A summary of the simulation is provided below, and further details may be found in Ref. [44]. These tools simulate the production of the Askaryan radio pulse resulting from neutrino interactions and propagate it through the ice and firn to the detector.

Neutrino interactions are simulated by forcing neutrinos to interact within a fiducial volume and weighting the resulting events by the probability with which they would occur. This probability accounts for neutrinos lost to absorption within the atmosphere and the Earth's crust, as well as tau neutrinos recovered due to ν_τ regeneration effects [45]. The neutrino-nucleon cross section follows the parametrization presented in Ref. [46], e.g. 1.45×10^{-32} cm^2 at $E_\nu = 10^9$ GeV. As ARIANNA stations are designed to be independent, simulations are focused predominately on calculating the response of a single ARIANNA station. For this purpose, the interaction volume is chosen to be a rectangular prism having a height 575 m, roughly equal to the ice thickness (see Sect. 1), and a horizontal cross section ranging from 3 to 10 km^2, depending on the neutrino energy. Consistent ice depth measurements at multiple locations, separated by 1 km, have been performed at the ARIANNA site [34]. These measurements have motivated the use of a simple uniform ice thickness model in the simulations. The neutrino interaction vertices are uniformly distributed within the fiducial volume and the neutrino arrival directions are isotropically distributed.

The neutrino energy is selected randomly according to a specified flux. For the results presented in this article, the ESS cosmogenic flux [38] described in Sect. 2.2.2 has been used. Neutrinos of each flavor have been simulated with equal arrival rates, consistent with the 1:1:1 flavor ratio expected of neutrinos generated by pion decay at distant sources [47]. Roughly two-thirds of the neutrinos undergo a charged-current interaction, while the remainder interact via the neutral current. The fraction of the neutrino energy carried over to the resulting hadronic shower, the inelasticity y, is randomly chosen following the distributions presented in Ref. [48]. This leads to an average inelasticity of 20% for cosmogenic neutrinos in the energy range of interest to ARIANNA.

The maximum strength of the electric field is parametrized [33] on the Cherenkov cone 1 m from the neutrino interaction vertex. This field strength is proportional to the fraction of neutrino energy deposited into the hadronic shower. The strength of the electric field at angles off the Cherenkov cone, $\delta\theta_c$, is parametrized by a Gaussian whose width is calculated according to Ref. [49] for hadronic and Ref. [50] for electromagnetic showers.

For charged current ν_e interactions, the field strength is increased by radiation from the prompt electromagnetic shower. For such interactions at energies above $\sim 10^9$ GeV, however, the longitudinal shower profile increases faster than $\log E_{\nu_e}$, rising as fast as $\sqrt{E_{\nu_e}}$ [51]. These elongated showers lead to a sharper reduction of the electric field strength at angles off the Cherenkov cone. This Landau-Pomeranchuk-Migdal (LPM) effect is simulated by reducing the Gaussian width of the Cherenkov cone spread by an amount proportional to $E_{\nu_e}^{-1/3}$.

The electric field is then propagated from the neutrino interaction vertex to the detector. The ice is modeled by a 75 m firn layer atop a 500 m ice shelf. The bulk ice is taken to have a refractive index $n = 1.78$ [52]. The index of refraction in the firn layer is calculated as a function of depth using the Schytt model [53] combined with previous ice core measurements taken from the Ross Ice Shelf [54], varying from $n = 1.30$ at the surface to $n = 1.78$ in the ice.

Radio signals propagating through the ice are attenuated by a factor that depends only on column depth. The frequency dependence of the attenuation length is averaged over the bandwidth of the LPDA, taken to be around 100 MHz to 1 GHz [55]. The variation of attenuation length with depth arises from the changing temperature of ice with depth, ranging from roughly -30° C at the surface of the ice to -2° C at bottom of the ice shelf. This depth variation results in an average attenuation length of 400 ± 18 m. Further power may be lost for radio pulses reflecting off the ice-seawater boundary. The simulations halve the power of the pulse (-3 dB) upon reflection, although in situ measurements show the reflectivity, R, of the boundary to be between $\sqrt{R} = 0.82 \pm 0.07$ [34].

2.1.2. Time Domain

The time domain response of the detector has been studied by constructing a collection of "waveform templates" that quantify the voltage measured by an antenna over time for an Askaryan radio pulse. Each waveform template is calculated for a radio frequency (RF) pulse arriving at a particular angle with respect to the antenna, as well as for a particular observation angle $\delta\theta_c$ relative to the Cherenkov cone.

The electric field produced by the Askaryan effect in ice is calculated as a function of time [56, 57] for an electromagnetic particle shower of a specified energy. The charge excess is modeled as a pancake with a charge profile that varies as the shower propagates. The effect of the lateral structure of the particle shower on the electric field is parametrized as a function of time using a form factor obtained from shower simulations [33].

The measured responses of the ARIANNA amplifier and LPDA are convolved with the electric field in order to produce the voltage observed by an antenna as a function of time. The propagation of the electric field through the ice reduces the strength of the field, but has a negligible effect on the relative frequency content compared to the impact of the hardware response. The antenna response is quantified in bins of two angles, both relative to boresight: one in the plane of the tines (the E-plane) and one normal to the plane of the tines (the H-plane).

Full details of the procedure used to calculate the time-dependent waveform templates may be found in Ref. [55].

2.2. Expected Performance

The properties of neutrino interactions that produce a radio pulse at a station with sufficient power to trigger the detector have been studied. Studies of the angular and energy resolution of ARIANNA are performed using a simulation of an eight downward LPDA station configuration. Simulated stations are triggered when the observed radio signal is larger than four times the noise on at least three out of the eight downward facing antennas. This threshold level has been achieved in situ with stations running a two out of four antenna channel trigger (see Sect. 3.2).

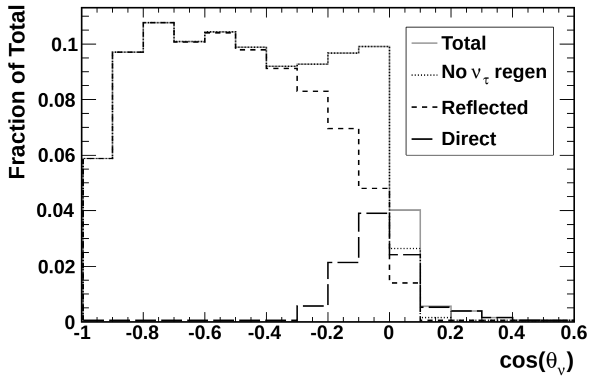

Figure 2: The number of neutrino triggers observed in each bin relative to the total number of cosmogenic [38] neutrino triggers as a function of the local zenith neutrino arrival angle. The station triggers on neutrinos arriving from the horizon through either direct or reflected radio pulses. The majority of triggers are due to reflected pulses from locally down-going neutrinos. Figure adapted from Ref. [44].

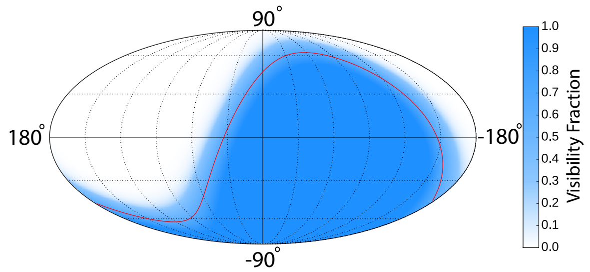

Figure 3: The angular coverage in Galactic coordinates. The color scale represents the fraction of livetime that a patch of the sky is visible. The solid line shows the sky visible to an ARIANNA-like detector at the South Pole.

2.2.1. ARIANNA Aperture

Neutrinos that trigger an ARIANNA station arrive predominately from the sky above the station, creating a radio pulse that reflects off the ice and water interface at the bottom of the ice shelf. Figure 2 shows the relative sensitivity of an ARIANNA station to neutrinos, averaged over flavor, as a function of local zenith angle. In addition to down-going neutrinos, ARIANNA is also sensitive to neutrinos arriving from the horizon. Such events may be triggered either through a reflected pulse or by a direct observation of the Cherenkov wavefront, depending on geometry.

The portion of the sky that ARIANNA observes with this angular sensitivity is shown in Galactic coordinates in Fig. 3. The line in the figure rep-

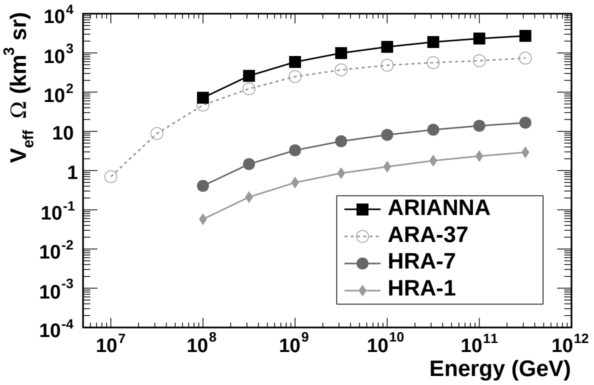

Figure 4: The effective volume times total viewing angle, at the trigger level with 4σ thresholds, of a 1296 station ARIANNA telescope as a function of energy. The effective volumes are averaged over neutrino flavors as well as over neutrinos and anti-neutrinos. Also shown are the $V_{eff}\,\Omega$ for a single HRA station, a seven station HRA, and the ARA-37 detector [24].

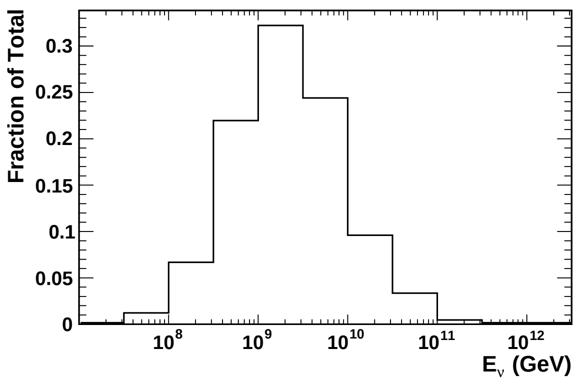

Figure 5: The number of neutrino triggers observed in each bin relative to the total number of cosmogenic [38] neutrino triggers as a function of the true simulated neutrino energy. Figure adapted from Ref. [44].

resents the view of an ARIANNA-like detector located at the South Pole. Note that the local zenith acceptance of an ARA-like detector falls off rapidly for neutrinos originating more than 45° above the detector [24]. Thus, an ARA-like detector would have reduced visibility of the sky around the southern polar region.

The effective volume of the full ARIANNA telescope in which neutrino interactions will be triggered has been studied as a function of energy, presented in Fig. 4, and is compared to that of the ARA-37 experiment [24]. The effective volume

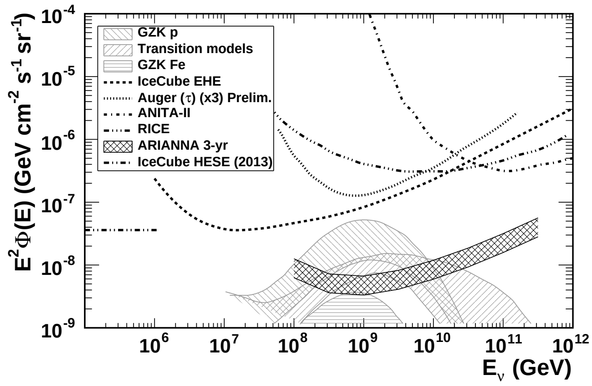

Figure 6: The all flavor $\nu + \bar{\nu}$ differential sensitivity of a 1296 station ARIANNA telescope running for 58% of three years with a signal efficiency of 83% (see Sect. 4.4). The sensitivity is calculated in a sliding decade-wide neutrino energy bin. See text for a discussion of the width of the sensitivity band. Limits on the flux of neutrinos are shown for several experiments [58–61], with ANITA [15, 16] providing the most stringent limits at the highest energies and IceCube [12] at lower energies. The cosmogenic neutrino flux predicted by several models is shown for different assumptions of the cosmic ray composition [37].

shown in Fig. 4 is integrated over the viewing angle of ARIANNA, allowing the expected number of neutrino triggers due to a neutrino flux, Φ, to be calculated as

$$dN(E) = \Phi(E)\,\frac{\varepsilon V_{eff}(E)\,\Omega}{L_{int}(E)}\,t_{live}\,dE \qquad (1)$$

where dN is the number of neutrinos in an energy bin, E is the average neutrino energy in the bin, dE is the width of the bin, ε is the efficiency with which neutrino triggers are preserved by an analysis, V_{eff} is the effective volume at the trigger level, Ω is the viewing angle in steradians, L_{int} is the water-equivalent interaction length of neutrinos in the ice ($\approx 10^3$ km at 10^9 GeV) and t_{live} is the livetime of the experiment.

This effective volume leads to an energy distribution of cosmogenic neutrino triggers that has 90% of detected neutrinos between $10^{8.4}$ GeV and $10^{10.4}$ GeV, as shown in Fig. 5. On an absolute scale, the all flavor $\nu + \bar{\nu}$ sensitivity of ARIANNA to trigger on neutrinos is presented in Fig. 6. This sensitivity has been calculated for 1296 ARIANNA stations running for three calendar years, with a livetime equal to 58% of each calendar year, and a signal efficiency of 83% (see Sect. 4.4). The fractional livetime corresponds to stations powered by batteries and/or solar panels and is based on the observed behavior of previously and currently deployed prototype stations. The sensitivity is calculated as the average Neyman upper limit with an expected Poissonian background of 0.3 events (see Sect. 4.4); i.e. dN = 2.47 neutrinos in the sliding decade-wide energy bin.

The systematic uncertainty band on the sensitivity shown in Fig. 6 accounts for uncertainties on the models used to describe various physics processes in the simulations. The neutrino-nucleon cross section is calculated from parton distribution functions extrapolated to the as yet unmeasured low-x values appropriate for $E_\nu \geq 10^7$ GeV, an estimation that may over or underestimate rates. The simulation of the LPM effect does not fragment the charge excess into separate clumps, which would give rise to competing effects: a reduction of the overall RF signal strength and an increase of the relative amplitude at angles away from the Cherenkov cone.

Other models employed by the simulations are understood to either increase or decrease expected rates. No RF contribution of the μ lepton arising from charged current ν_μ interactions is simulated, which underestimates trigger rates [42]. However, the ν_τ trigger rates are likely overestimated since the τ lepton resulting from a ν_τ interaction is not propagated. Instead, the shower with the greater energy, either from the ν_τ interaction or the τ decay (if it produces a shower), is simulated at the neutrino interaction location. Thus, τ lepton decays that produce very high energy showers outside the fiducial volume are allowed to trigger a station.

Uncertainties on the ice properties used in the simulations also contribute to the sensitivity band. Simulated pulses lose half their power upon reflection, however measurements at the site suggest a significantly larger reflection coefficient. Similarly, ice property measurements at the site suggest the RF signal loss due to refraction and attenuation in the firn layer is likely overestimated.

2.2.2. Expected Neutrino Rates

The number of neutrino triggers that ARIANNA can expect to record after 3 calendar years of running is presented in Table 1 for a variety of neutrino flux models. Unless otherwise stated, neutrino fluxes are generated through photopion production by a flux of cosmic rays. The evolution of cosmic ray sources follows the evolution of potential source populations, such as the star formation history. This is typically approximated by an increasing emissivity per co-moving volume proportional to $(1+z)^m$ out to a first break point at $z = z_{max}$, where z is the redshift of the source.

The ESS model [38] shown in Table 1 assumes cosmic sources evolve with $m = 4$ and $z_{max} = 1.9$ in a flat universe. The WB model [62] follows the luminosity density evolution of quasi-stellar objects (QSOs) with $m = 3$ for $z_{max} = 1.9$. The Yuksel *et al.* [63] model parameterizes a very strong source evolution according to the gamma ray-burst (GRB) rate, with $m = 4.8$ up to $z_{max} = 1$. Three of the Kotera *et al.* [64] models vary the source evolution of a flux of protons, with $m = 3.4$ up to $z_{max} = 1$ for a star formation rate (SFR1) evolution. The GRB2 model from Kotera *et al.* closely follows the SFR1 evolution, but continues to gradually increase beyond $z > 4$. The Kotera *et al.* FRII model employs a very steep evolution out to $z_{max} = 4$. The Yoshida and Teshima [65] also assumes a strong evolution, $m = 4$, out to $z_{max} = 4$. The Ahlers *et al.* [66] models take $m = 4.6$ until $z_{max} = 2$ and constrain the energy spectra of particles injected to the cosmic ray accelerating source using gamma ray measurements taken by the Fermi-LAT. The cross-over energy between galactic and extragalactic cosmic rays is parameterized by a lower energy break in the injection spectra of $E_{min} = 10^{10}$ GeV.

The possibility of a chemical composition of the cosmic ray flux that is not purely proton is also explored. The Kotera *et al.* mixed composition model assumes that the chemical composition of particles injected to the cosmic ray source matches the composition of the low energy galactic cosmic ray flux. The Kotera *et al.* pure iron model tests the case of a purely iron nucleus composition. In both cases, the sources evolve according to the SFR1 parameterization. The Ave *et al.* [67] model also uses a purely iron composition, but includes a stronger source evolution of $m = 4$ out to $z_{max} = 1.9$. The Olinto *et al.* [43] tests a purely iron composition combined with a uniform source evolution and a cutoff in the source acceleration at $E_{max}/Z = 10^{11}$ GeV.

The Aartsen *et al.* [23] flux represents the best fit to the neutrino flux measurement obtained by the IceCube collaboration after the observation of 37 neutrino candidate events with energies up to 2 PeV. A measurement of this flux by ARIANNA would extend the currently measured spectrum to higher neutrino energies by at least two orders of magnitude.

ARIANNA can also search for alternative sources of UHE neutrinos such as young pulsars that accelerate particles through surrounding supernova rem-

Neutrino Model	Model Type	N_ν Triggers ($E_\nu > 10^8$ GeV)	
		ARIANNA	IceCube [12]
ESS (2001) [38]	$m = 4$, $\Omega_M = 1$	55	
WB (1999) [62]	E_ν^{-2} QSO source evolution	65	
Yuksel *et al.* (2007) [63]	E_ν^{-2} GRB source evolution	100	
Kotera *et al.* (2010) [64]	Protons, SFR1 evolution	7.3	0.46 (0.64)
Kotera *et al.* (2010) [64]	Protons, GRB2 evolution	9.0	0.48 (0.67)
Kotera *et al.* (2010) [64]	Protons, FRII evolution	48	2.9 (4.0)
Yoshida *et al.* (1993) [65]	$m = 4$, $z_{max} = 4$	34	2.0 (2.8)
Ahlers *et al.* (2010) [66]	$E_{min} = 10^{10}$ GeV (best fit)	26	1.5 (2.1)
Ahlers *et al.* (2010) [66]	$E_{min} = 10^{10}$ GeV (maximal)	58	3.1 (4.3)
Kotera *et al.* (2010) [64]	Mixed composition	7.4	
Kotera *et al.* (2010) [64]	Pure Iron	2.5	
Ave *et al.* (2005) [67]	Pure Iron, $m = 4$, $z_{max} = 1.9$	18	
Olinto *et al.* (2011) [43]	Pure Iron, $E_{max}/Z = 10^{11}$ GeV	0.097	
Aartsen *et al.* (2014) [23]	$E_\nu^{-2.3}$ IceCube best fit	2.8	
Fang *et al.* (2013) [68]	Young pulsar sources	43	

Table 1: The expected number of triggers due to neutrinos of all flavors with $E_\nu > 10^8$ GeV in 1296 ARIANNA stations after running for 3 calendar years given different models of the cosmogenic neutrino flux. A flavor ratio of 1:1:1 at Earth is assumed. A realistic livetime of 58% per year and a signal efficiency of 83% (see Sect. 4.4) has been used for the ARIANNA rates. See text for an explanation of the model types. For reference, if 0.3 background events are expected in the data set (see Sect. 4.4), 6.4 neutrino events would push the number of observed events beyond a 5σ background fluctuation in 50% of experiments (prior to any trial factor penalties). Published neutrino rates for IceCube with 333.5 days of IC40, 285.8 days of IC79 and 330.1 days of IC86 data [12] are shown where available. The numbers in parentheses show the IceCube rates increased by 39% to facilitate direct comparison with the ARIANNA 3 year rates.

nant material, as modeled by Fang *et al.* [68]. In this model, sources evolve according to the star formation rate.

ARIANNA can expect to see about 13 times as many neutrinos above 10^8 GeV as IceCube, depending on the flux model, and a comparable number of neutrinos to ARA [24] for similar model parameters. This increase in sensitivity relative to current limits will create the opportunity to study nearly all mixed composition models (currently favored by Auger data) that include a power law injection spectrum, and to probe alternate scenarios of cosmic ray acceleration such as young pulsar sources.

2.2.3. Angular Resolution

The angular resolution of an ARIANNA station has been estimated through the use of a simple reconstruction procedure on simulated neutrino events. The arrival direction of the radio pulse is found by fitting the time difference between pulses in different antennas, on a single ARIANNA station, to a planar wavefront. Thanks to the better than 100 ps timing of ARIANNA stations [69], the angular error on the direction of the RF signal at the station is better than 1° [70].

To determine the direction of the neutrino, however, it is necessary to estimate both the signal propagation direction as well as the signal polarization direction. For example, a signal arriving vertically upward and on the Cherenkov cone would be produced by a neutrino with a zenith angle equal to the Cherenkov angle. Any azimuth angle would produce the same upward propagating signal. The polarization angle serves to break this degeneracy, as the polarization is perpendicular to the signal propagation direction and points away from the shower axis.

An ARIANNA station with eight downward-facing LPDAs has been simulated in order to quantify the neutrino angular resolution. The polarization of the incoming radio pulse is determined by the relative amplitude of the pulses recorded by non-parallel antennas. The voltage recorded by an antenna is proportional to the component of the electric field vector in the direction parallel with the tines of the LPDA. The constant of proportionality depends on the incoming direction of the radio signal and on the in-ice antenna response.

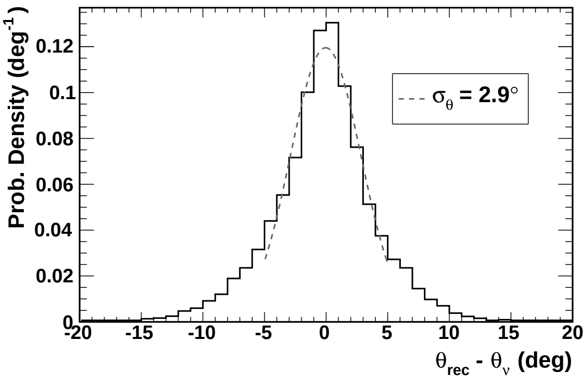

Figure 7: The angular difference between the reconstructed and true neutrino direction in the local zenith direction. A resolution of $\sigma_\theta = 2.9°$ is found for an eight-antenna ARIANNA station. Figure adapted from Ref. [44].

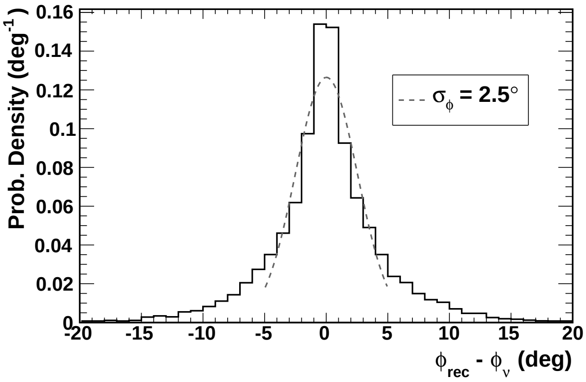

Figure 8: The angular difference between the reconstructed and true neutrino direction in the local azimuth direction. A resolution of $\sigma_\phi = 2.5°$ is found for an eight-antenna ARIANNA station. Figure adapted from Ref. [44].

The polarization is reconstructed by first finding the antenna with the largest recorded pulse. The voltage recorded by each of the two adjacent antennas is then used to obtain the magnitude of the electric field component that is parallel to the tines of that antenna. The ratio of these electric field components gives the tangent of the azimuth angle of the polarization vector (the component in the plane of the ice surface). The reconstruction is improved by averaging the signal of each antenna with its parallel counterpart antenna prior to calculating the ratio. This improves the signal to noise of the measurement of each electric field component and gives a more accurate estimate of the azimuth angle of the polarization vector.

The zenith angle of the polarization vector is then constrained by the requirement that the polarization and signal propagation vectors be orthogonal. This yields two degenerate polarization vectors, each having the same azimuth angle and each being perpendicular to the signal propagation. Given that only the signal propagation vector is needed to measure the energy of the neutrino, this degeneracy does not affect a measurement of the diffuse neutrino flux. For point source searches, however, it will result in two possible neutrino source directions. The correct degenerate direction will always roughly point back to the source, while the incorrect degenerate direction will vary depending on the station orientation (and time). Thus, only a single point of excess signal would be expected for a given neutrino source.

The angular resolution expected for this method is shown in Figs. 7 and 8. The resolution is calculated using the more accurate (compared to the true direction) of the two degenerate candidates, since this is the relevant quantity for a neutrino point source search. The local zenith and azimuth angular resolutions are $\sigma_\theta = 2.9°$ and $\sigma_\phi = 2.5°$, respectively.

These values are conservative, in that they have been obtained by a reconstruction that assumes that each antenna is observing the electric field exactly at the Cherenkov cone, i.e. $\delta\theta_c = 0$. In fact, on average $\delta\theta_c$ is found to be about 2.2°, and some triggers are produced by antennas observing signals up to 15° off-cone. The assumption that all signals are on the Cherenkov cone is a major source of inaccuracy in the reconstruction of the neutrino direction. Determining the $\delta\theta_c$ to within 1.5° improves the neutrino direction angular resolution by over 50% in zenith and over 20% in azimuth.

2.2.4. Energy Resolution

The energy of an individual neutrino event is reconstructed by determining the strength of the electric field at the station and propagating it back through the ice to the shower location. The shower energy is proportional to the amplitude of the electric field at the shower. The constant of proportionality is calculated using measured antenna response properties. The energy of the original neutrino is then estimated using the average fraction of neutrino energy transferred to a shower that results in a trigger. The trigger requirement selects a subset of neutrino interactions for which a large fraction of

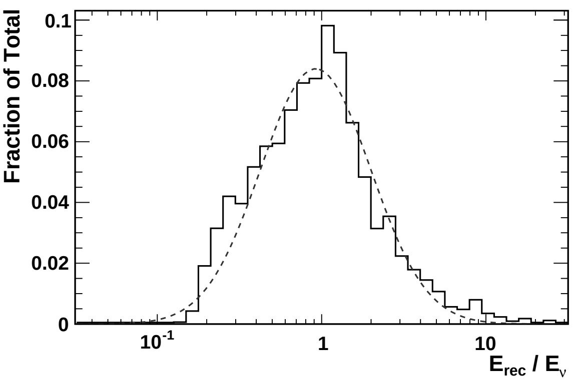

Figure 9: The energy resolution of an eight-antenna ARIANNA station to a cosmogenic flux [38] is $\sigma(\log(E_{rec}/E_\nu)) = 0.34$, so that $\sigma(E_{rec}/E_\nu) = 2.2$ for cosmogenic neutrinos, summed over neutrino flavor. Figure adapted from Ref. [44].

the energy, about 0.8, is transferred to the shower. An average path length of radio pulses is used in lieu of a shower vertex reconstruction. The average path length is determined from simulations as a function of the zenith angle of the radio signal propagation, which itself is readily determined using timing (see Sect. 2.2.3).

There are two dominant sources of error on the neutrino energy estimate. The first arises due to the Gaussian dependence of the electric field amplitude on $\delta\theta_c$. Uncertainties on $\delta\theta_c$ form the largest source of error on the energy estimate. The unknown amount of energy transferred from the neutrino to the charged particle shower is the second significant source of error on the energy estimate. The distribution and average value of these two parameters depend on neutrino flavor, which is assumed to be unknown in the current analysis. As more sophistication is applied to event reconstruction, it should be possible to identify the flavor and thereby improve the energy resolution. Errors due to the inexact pulse propagation length, electric field losses due to reflection at the ice and water boundary and inaccuracies in the antenna response are each on the order of 20-25%, and are negligible by comparison.

In the analysis presented here, there is no attempt to determine the angular deviation from the Cherenkov cone, $\delta\theta_c$. Inserting the average value obtained from simulation studies, the energy resolution is found to be $\sigma(E_{rec}/E_\nu) \approx 5$, under the assumption that $E_{sh}/E_\nu = 0.8$ for triggered events, where E_{sh} (E_ν) is the energy of the shower (neutrino). However, because the frequency and phase content of the Askaryan pulse depends on $\delta\theta_c$, it can be exploited in future analyses to reduce this uncertainty. Such a potential measurement of $\delta\theta_c$ has been modeled in Ref. [44] in order to investigate the reduction in energy resolution. The result of this study is shown in Fig. 9, which indicates that the average neutrino energy resolution is reduced to $\sigma(E_{rec}/E_\nu) = 2.2$, an improvement by a factor greater than 2.

2.3. Cosmic Ray Detection

Ultra-high energy cosmic rays are a plausible source of (reducible) background for ARIANNA. Charged particle showers in the atmosphere above the telescope, produced by UHE cosmic rays, can emit a detectable radio pulse. Much of this background is reduced naturally by the 15 dB decrease in sensitivity of the LPDA back lobe relative to boresight. The addition of two upward facing antennas eliminates the remaining cosmic ray background. These antennas allow RF pulses originating from the atmosphere to be efficiently distinguished from neutrino pulses originating in the ice.

Dedicated cosmic ray simulations have been performed to study the rate at which an ARIANNA station triggers on air showers and the efficiency with which such events are separated from neutrino events. The simulation of the cosmic ray air showers are performed using the CoREAS software [71–73]. Proton interactions between $10^{8.4}$ and $10^{10.5}$ GeV are simulated by Corsika [74] using the QGSJetII-04 [75] hadronic model and weighted by the high energy cosmic ray flux measured by the Auger experiment [76].

Cosmic rays are studied over a local zenith angle range from 0°-75° under the assumption of an isotropic flux. The azimuth direction and interaction vertex position relative to the station are varied for each combination of energy and zenith direction.

The radio pulse from the charged particle shower is generated and propagated to the surface of the ice by CoREAS. The electric field at the station in the frequency domain is convolved with the measured ARIANNA antenna response, the result of which is then convolved with the measured amplifier response to obtain the voltage expected on each readout channel of the DAQ. A trigger is generated if the signal in three or more of the eight downward facing antenna channels is above four times the noise (4σ). This is the same trigger criteria used in Sect. 2.2 to study neutrino signals. Finally, finite

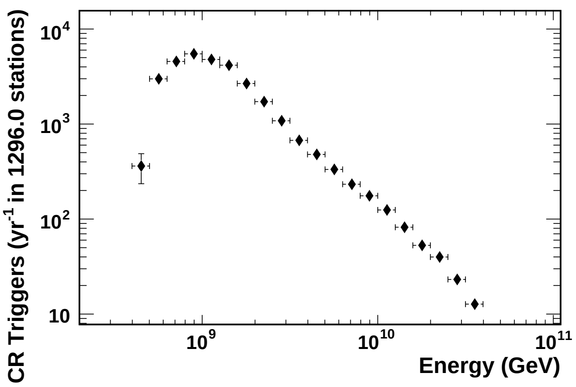

Figure 10: The number of triggered cosmic ray events in 1296 ARIANNA stations per calendar year, with a livetime of 58% per year, versus the cosmic ray energy, in tenth of a decade energy bins.

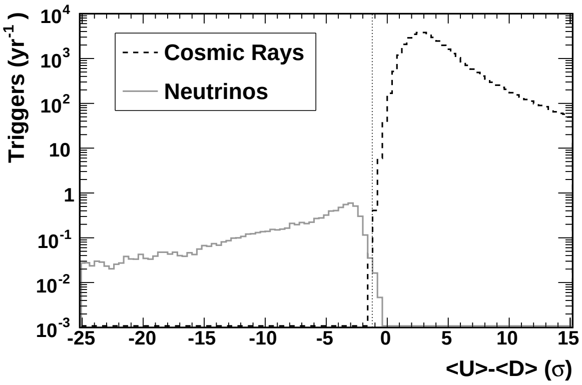

Figure 11: The number of triggered neutrino and cosmic ray events in 1296 ARIANNA stations per calendar year versus the difference in the average amplitude of upward facing antennas and the average amplitude of downward facing antennas. Requiring the difference to be $< -1.2\sigma$ yields a background rate of 0.1 cosmic rays in 3 calendar years of data from the full array while preserving 99.7% of the triggered neutrino events. The neutrino rate is arbitrarily scaled to 10 ν per year for illustration purposes.

bandwidth noise consistent with that observed by HRA stations is added to the signal. The trigger is applied prior to the addition of noise in order to avoid over-counting due to events that will be rejected by any analysis.

The rate of cosmic ray triggers in the full ARIANNA telescope is shown in Fig. 10 as a function of cosmic ray energy. The rates are shown as the expected number of triggers per calendar year in each (tenth of a decade) energy bin. A detailed measurement of the backward lobe response of the LPDA has not yet been performed, so a conservative estimate of the cosmic ray rates has been obtained by overestimating the gain of the antennas for signals arriving from above the detector.

To study the reduction of this potential background, a ten LPDA station has been simulated for the cosmic ray studies. This station has eight downward facing antennas (see Sect. 2.2). In addition, two upward facing LPDAs have been added to the station geometry to help discriminate between RF pulses arriving from above or below the station. These two antennas are oriented upward at a 45° angle relative to the surface of the ice and do not participate in the trigger. This geometry is shown in Fig. 1.

The difference between the pulse amplitudes measured by the upward and downward facing antennas provides an efficient mechanism for distinguishing cosmic ray air showers from neutrino signals. On each antenna, the amplitude is taken as the average of the two largest crests of the time dependent waveform in order to reduce fluctuations due to noise. Figure 11 shows the average upward facing antenna amplitude minus the average downward facing antenna amplitude for both cosmic ray and neutrino events. Keeping only events with an amplitude difference $< -1.2\sigma$ leads to a background rate of 0.1 cosmic rays in the full 1296 station ARIANNA telescope after 3 calendar years of running with 58% livetime per year. This cut preserves 99.7% of the cosmogenic neutrino events that trigger the station.

3. The Hexagonal Radio Array

The ARIANNA Hexagonal Radio Array (HRA) is being constructed on the Ross Ice Shelf and consists of seven prototype stations arranged as shown in Fig. 12. This small array, begun in 2009 [77], serves as a prototype for the development and study of ARIANNA hardware, data acquisition (DAQ) and radio data analysis. Three stations have been installed at the ARIANNA site, Stations A, C and G, to form the HRA-3 detector. The fourth station, Station D, is of a preliminary design installed during the 2011-2012 austral summer [78]. This station did not take radio event data during the 2013-14 season as its DAQ electronics were removed from the station for calibration. A search has been performed for cosmogenic neutrino signals using data

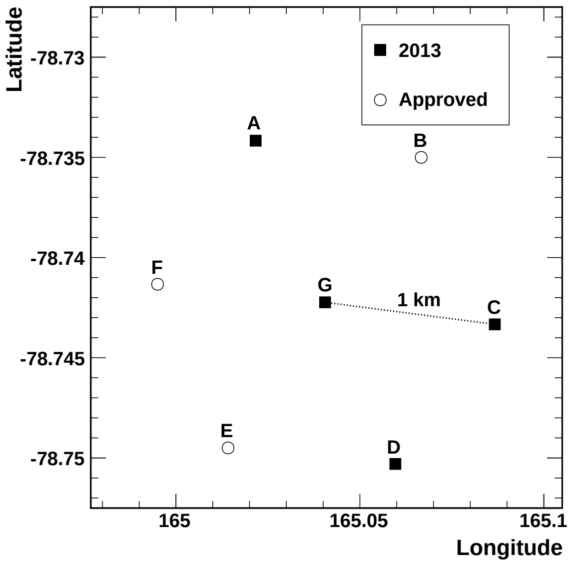

Figure 12: The locations of the seven Hexagonal Radio Array stations. The HRA-3 station locations are shown by the closed squares marked "A", "C" and "G", an earlier prototype station location is marked "D", while the approved sites of the remaining four stations by open circles. Figure from Ref. [69].

taken by the HRA-3 during the 2013-14 deployment season.

3.1. The HRA-3 Stations

Three stations have been used to collect radio data during the 2013 deployment season. Each station consists of four downward facing LPDAs connected to a local DAQ. The radio antennas are positioned symmetrically around the DAQ box which lies at the center. Each antenna is 3 m from the DAQ and is oriented such that the normal vector of the plane containing the antenna tines points toward the DAQ. The data acquisition is able to transmit data from Antarctica in near real-time while drawing an average of only about 7 W.

Radio signals measured by the LPDAs are amplified and digitized at the data acquisition box. Signals are carried to custom amplifiers through heavily shielded coaxial cables. The output of each amplifier is then sampled at 1.92 GHz using a custom Advanced Transient Waveform Digitizer (ATWD) chip [79]. The chip records waveform data in 128 samples and voltages are digitized using 12 bit analog to digital converters.

Two complementary communication systems are used to transfer data taken by a station to off-site locations. These systems are powered off during data taking in order to minimize radio noise and to conserve power. A long range wireless Ethernet link is facilitated by an AFAR modem [80] that connects to the Internet via a relay positioned on Mt. Discovery and a receiver at McMurdo Station. Each station is also equipped with an Iridium Short Burst Data (SBD) modem [81] that allows 320 byte binary messages to be sent via satellite when an AFAR connection cannot be established.

Station configuration parameters, such as trigger thresholds, are specified remotely by shift crews and transmitted to the stations using the communication peripherals. Each station periodically connects to computers in California in order to transmit diagnostic data. During the connection, radio event data may be transferred and new configuration parameters may be specified. This facilitates near real-time data analysis and station monitoring throughout the data taking season.

During the 2013 deployment season, events were recorded by an HRA-3 station when the time-dependent waveforms on two of four antenna channels matched a pattern trigger. The coincidence is required to occur within 64 ns. The pattern requires the crossing of both positive and negative 4σ thresholds and is efficient for bipolar pulses of frequencies within the LPDA and amplifier bandwidths. The bipolar pulse requirement reduces triggers on random electronics noise while preserving those due to neutrino-induced Askaryan pulses, as the finite bandwidth of the LPDA and amplifier will always yield a bipolar pulse (due to ringing).

To facilitate studies of the thermal environment noise, the collection of data at random times is facilitated by software forced triggers. The stations typically record such an "unbiased" event once every 67 seconds.

A detailed description of the HRA-3 power, communications and data acquisition hardware and performance may be found in Ref. [69].

3.2. Operation of the HRA-3

The HRA-3 stations installed in the 2013 deployment season took data until the lack of solar power caused the batteries to deplete in April, 2014. The communication systems functioned as expected during the entire data taking season. Connections over the wireless internet link began to fail in early April due to the loss of reliable power at the relay on

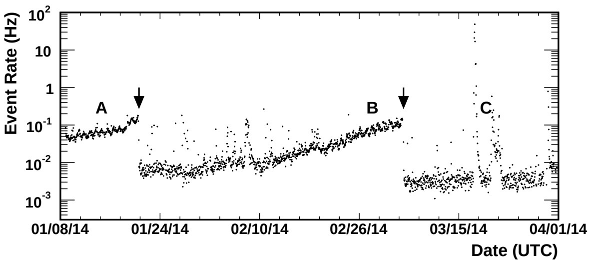

Figure 13: The rate of thermal triggers over time for Station A. The letters indicate periods in which different features are seen in the rates. During periods A and B, both the small diurnal variations in rate as well as the overall gradual increase in rate is due to variations in the temperature of the amplifiers. The arrows indicate the two adjustments made to the trigger thresholds. During period C, a large storm passed through the ARIANNA site, resulting in large fluctuations of the trigger rate. Figure from Ref. [69].

Mt. Discovery. Satellite connections over the Iridium network continued to function until the loss of station power in mid-April.

The bipolar trigger requirement on two of four antenna channels, described in Section 3.1, allowed the stations to run at low trigger rates while also keeping thresholds low. As shown in Fig. 13, the trigger rate of Station A was typically below 0.1 Hz and an average rate of 10^{-3} Hz has been achieved with 4σ thresholds.

Several features in the triggering rates can be found in Fig. 13 during the periods marked by the letters. Small diurnal trigger rate fluctuations seen in periods A and B are attributed to daily temperature variations of the amplifiers. The gradual increasing of the trigger rate during period B is caused by an overall cooling of the amplifier electronics. This cooling raised the gain of some amplifiers more than others, leading to different effective thresholds on different channels and allowing small diurnal temperature fluctuations to affect trigger rates during period B. Once the station is fully buried in snow and thresholds are balanced, the trigger rates are found to be stable. Such periods are observed after each threshold tuning, marked by the arrows. Other HRA-3 stations exhibited a similar dependence of trigger rates on temperature.

The typical observed thermal trigger rates match the rates expected for the threshold values. The trigger thresholds were only adjusted twice during the 2013-14 data taking season, denoted by the arrows in Fig. 13. The threshold adjustments primarily served to re-balance the single-channel trigger rates. This allows each channel to participate equally in the trigger requirement that at least two out of four antenna channels have significant bipolar signals.

An increase in the trigger rate during storms at the ARIANNA site has been observed. One such period, marked as period C, is visible in Fig. 13. The precise cause of these triggers continues to be investigated. During periods of high wind speeds, above roughly 20 knots, a correlated rise in rates among all stations is seen. However, not all high wind periods result in elevated trigger rates. The events recorded during these periods are readily distinguishable from expected neutrino signals, as discussed in Sect. 4.

4. Search for Neutrino Signals in HRA-3 Data

4.1. The Data Set

Data taken by the HRA-3 between January 3 and April 9, 2014 has been analyzed to search for neutrino-induced Askaryan signals. The former date corresponds to the departure of the deployment crew from the Ross Ice Shelf. The latter date is chosen to include all data successfully transferred off of Antarctica. The entire data set taken by the HRA-3 and transferred off site is included in the analysis, resulting in a combined livetime for the three stations of 170 days.

The bulk of the livetime deficit is not attributable to operational deadtime. Towards the end of March, the wireless Internet connection to the stations became less reliable, and a significant portion of the data set taken during this period remained on the stations. With the resumption of operations in the austral summer, the remaining data will be transferred off site and added to the data set for analysis. In addition, the continuous taking of radio data by Station G was halted during a period of severe weather at the site just prior to midnight, February 12, 2014 (UTC). An unnecessary diode train (not present on other stations) between the solar panel and battery of the station failed, breaking the electrical connection between the two. To conserve battery power, a short period each day was used to collect radio data. The station was otherwise kept in a low power configuration during which the battery power supply was monitored. The station continued to operate for 3 months without external charging. Removal of the diode train during the following summer season allowed the station's batteries to charge.

The deadtime of each station during its normal data-taking operation was typically 6% or less. During such periods, each station takes radio data continuously, pausing only for periodic off site communications and for brief calibration data collection, as described in Sect. 3.1. The off site communications typically last for 1 minute and occur every half hour, accounting for a 4%-5% deadtime, depending on the connection stability. A deadtime of 1% results from the collection calibration data, performed for for 10 minutes every 12 hours. These two interruptions of radio data taking constitute the entirety of the station deadtime during normal operation. Deadtime due to triggering and data acquisition is negligible as trigger rates are far below the maximum acquisition rate. The intentional disabling of radio data collection, such as the low-power operation of Station G after its batteries were no longer able to be charged, has not been included in the calculation of the fractional deadtime observed during data taking.

4.2. Neutrino Candidate Selection

The search for neutrino signals in the data set has been performed using a simple analysis for which the reconstruction of the radio signal direction is unnecessary [82]. Neutrino candidate events are required to meet three criteria. First, the event should pass a filter designed to reject purely random thermal triggers. Second, the event should not show evidence of electronics noise characterized by sinusoidal waveforms. Third, to separate neutrino candidates from non-thermal background events such as those associated with strong winds, the waveform observed by at least one LPDA is required to correspond reasonably well to the waveform expected for a neutrino.

The impact of the cuts on neutrino signals has been estimated using simulations. Neutrino events are generated according to a cosmogenic flux energy distribution and radio signals are propagated to the detector station in the frequency domain, as described in Sect. 2.1.1. These simulated neutrino events are required to pass the same trigger requirement used in the HRA-3 data: at least 2 of 4 antennas must have bipolar signals beyond 4σ. The time-dependent waveform measured by an antenna is then determined by first choosing the appropriate neutrino waveform template (see Sect. 2.1.2) based on the relative orientation of the LPDA and

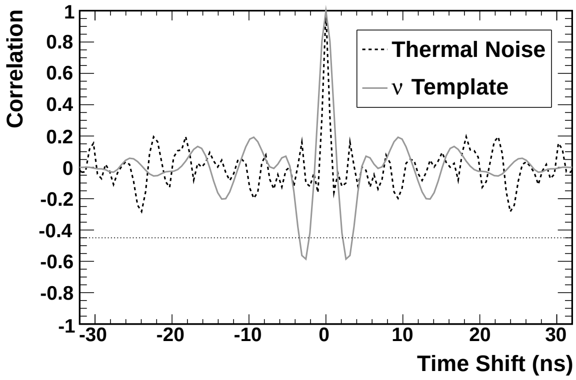

Figure 14: A comparison of the autocorrelation function for a purely thermal noise waveform (from a software forced trigger) and a neutrino template waveform. The dotted horizontal line shows the cut value ($\alpha < -0.45$) used in the analysis.

the incoming radio signal direction. Each template is then scaled such that its amplitude corresponds to that calculated by the frequency-domain simulation. Finally, finite bandwidth noise is added to each waveform.

Purely random triggers are identified in the data by noting that continuous white noise has an autocorrelation function with a perfect correlation at zero time offset, and no correlation at other time offsets. This property is used to distinguish purely random thermal triggers from non-thermal events. Figure 14 contrasts the autocorrelation of a waveform from a software forced trigger (purely thermal noise) with that of a waveform expected for a typical neutrino signal.

Non-thermal events are taken to be those for which the minimum value of the autocorrelation function, α, falls below -0.45 on any antenna. All other events are attributed to pure thermal noise. This requirement correctly identifies as purely thermal 99% of software forced triggers in the HRA-3 data set. Of the regularly triggered events (radio signals, thermal noise, etc.), 69% are identified as purely thermal. This filter is planned to be implemented locally on the stations as a real-time "level zero trigger." Such a level zero trigger will reduce event rates sufficiently to allow the near real-time transfer of radio event data from the full 1296 station ARIANNA detector using only low bandwidth Iridium SBD communications.

As expected, the autocorrelation cut rejects very few of the neutrino signal events, with 99.5% of the

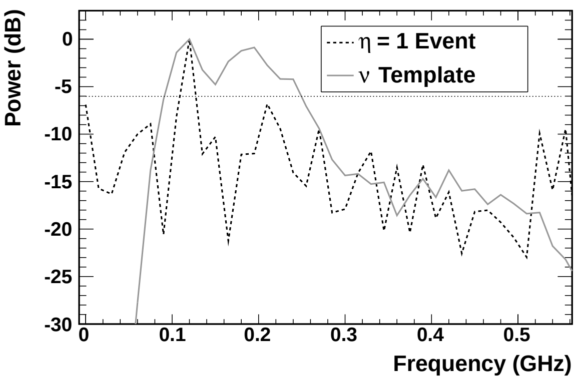

Figure 15: A comparison of the frequency spectrum of a non-thermal event that has a very low number of high magnitude frequency bins, in this case a single sharp peak at 120 MHz, and a neutrino template waveform with no noise. Each spectrum is normalized to have its peak power at 0 dB. The dotted horizontal line shows the cut value used in the analysis (-6 dB).

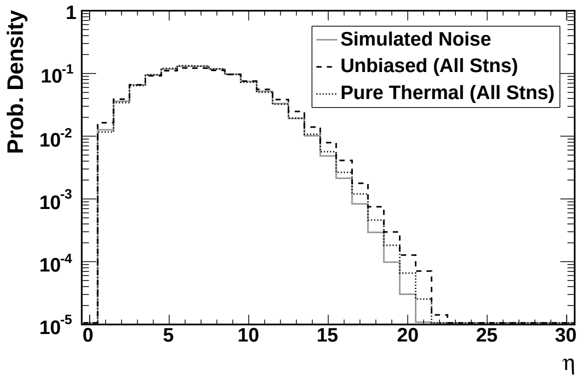

Figure 16: Comparison of the η distribution of pure thermal data, software forced (unbiased) triggered data and simulated finite bandwidth noise data.

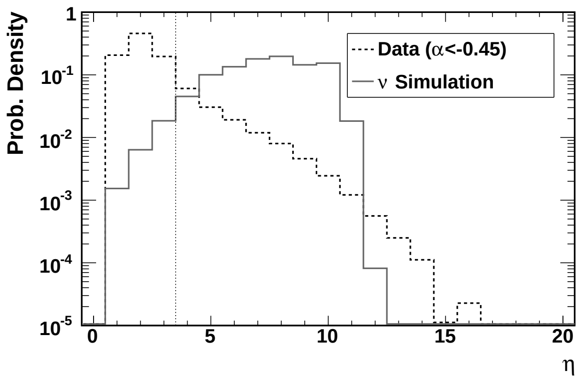

Figure 17: The η distribution of events in the data (of all stations) and the neutrino signal simulations. The cut, $\eta > 3$, is shown by the dotted vertical line. Only events with $\alpha < -0.45$ are shown for each population.

neutrino events having $\alpha < -0.45$.

Some non-thermal events are present in the data that resemble detector electronic noise rather than external radio noise. Such events are not associated with external conditions like high winds. Instead, they are characterized by strong sinusoidal waveforms and timing between antennas that is inconsistent with a physical external signal. While the latter property facilitates a powerful rejection based on signal direction reconstruction, the sinusoidal structure of the waveform is already sufficient to identify the events. These events are identified by a strong, narrow peak in the frequency spectrum of the waveform recorded by at least one antenna.

Figure 15 shows the frequency spectrum, measured in 10.6 MHz bins, of such a sinusoidal-like waveform compared to that expected for a typical neutrino signal. The frequency spectrum of a neutrino candidate waveform is required to have more than 3 frequency bins at or above half of the magnitude of the frequency bin containing the maximum magnitude. This variable is referred to as η. It is equivalent to the number of frequency bins containing more than one quarter of the maximum power.

The η distribution of the thermal noise data has been compared to the distributions in both software forced triggers as well as simulated finite bandwidth noise, as shown in Fig. 16. This comparison shows that the cut variable behaves as expected.

Events with a strong frequency peak, so that $\eta \leq 3$, are rejected as being due to detector noise. This cut removes 85% of the remaining non-thermal triggered events across all three stations. The $\eta > 3$ requirement also preserves the vast majority of neutrino signals, with 97% of the neutrino events passing the cut. The distributions of η in the neutrino signal simulations and in the data for events with $\alpha < -0.45$ are shown in Fig. 17.

The third and final neutrino candidate selection criteria requires that the waveform recorded in at least one antenna resemble that expected for a neutrino signal. This is done by calculating the maximum correlation value (for any time shift) between the waveform reported by an antenna with a reference neutrino signal template (see Sect. 2.1.2). The relative amplitude between the waveform recorded

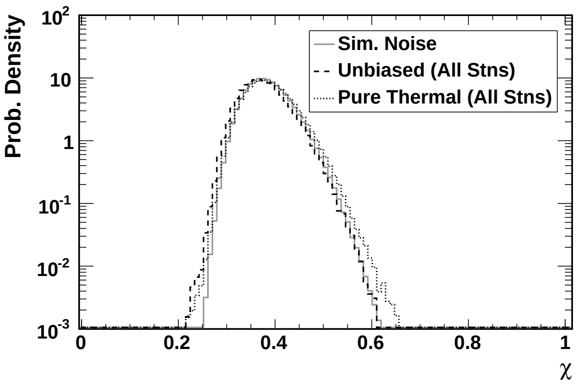

Figure 18: Comparison of the χ distribution of pure thermal data, software forced (unbiased) triggered data and simulated finite bandwidth noise data.

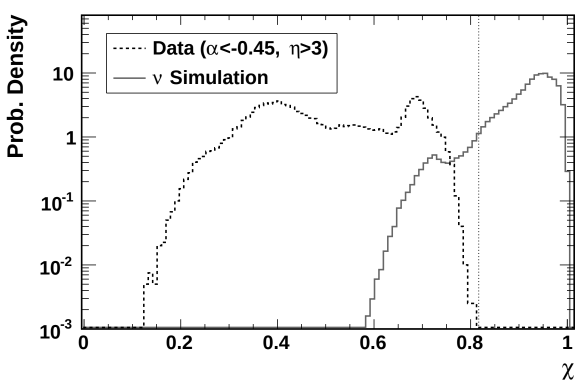

Figure 19: The distribution of χ in the data (of all stations) and the neutrino signal simulations. The cut, $\chi > 0.81$, is shown by the dotted vertical line. Only events with both $\alpha < -0.45$ and $\eta > 3$ are shown for each population. The peak in the data around $\chi \approx 0.68$ is due to events associated with high wind periods (see Fig. 20).

in the data and the neutrino template does not affect the Pearson correlation value [83].

As the signal direction is not reconstructed, the relative geometry of the signal direction and antenna orientation is not used to determine the proper neutrino waveform template to be used as a reference. Instead, the neutrino template corresponding to a signal arriving with local E-plane and H-plane angles (see Sect. 2.1.2) of 30° is taken as a reference for every antenna in every event. This reference was chosen as it represents the average relative geometry observed in the simulations.

The calculation of the correlation between a waveform and the reference neutrino template is complicated by the unknown relative polarity between the recorded signal and the reference template. For example, an LPDA with its tines oriented from East to West and its cable connector facing South may record a bipolar pulse with a *positive* initial crest for some incoming signal. On the other hand, rotating the LPDA by 180° so that its cable connector faces North, with its tines oriented from West to East, would result in a bipolar pulse with a *negative* initial crest being recorded for the same signal. To account for this effect, the correlation is calculated for all possible unique combinations of relative polarity between each antenna and the reference template. The best correlation found between the reference and any antenna, across all possible polarity orientations, is referred to as χ.

A comparison of the χ distribution of thermal noise data, software forced triggers and simulated finite bandwidth noise is shown in Fig. 18. This comparison shows that the χ variable behaves as expected.

Neutrino candidate events are required to have a $\chi > 0.81$. This seemingly large correlation value arises from the choice of cutting on the best correlation. As shown in Fig. 19, which compares the χ distributions of neutrino signal simulations and events in the data having both $\alpha < -0.45$ and $\eta > 3$, the cut value is not large compared to the correlation value expected for neutrino signals. None of the remaining events in the data set survive the $\chi > 0.81$ requirement. The requirement that $\chi > 0.81$ preserves 93% of the remaining signal events.

Figure 20 shows the χ value as a function of time for events with $\alpha < -0.45$ and $\eta > 3$. The band of events with $\chi \approx 0.4$ is formed by purely thermal events that survive the rather loose autocorrelation cut. Threshold tuning, indicated by the arrows, results in a sharp reduction of these events. Although each station had its threshold tuned only twice, different stations were tuned at different times. An increase in non-thermal background events is clearly seen during high wind periods, indicated by the labels "A" and "B." While background rates increased on all stations during these storms, Station G recorded many more background events than the other two stations during the storm indicated by label A. It was during this storm that the batteries of Station G stopped receiving charge. This period accounts for both the larger number of background events taken by Station G as well as the peak in the

	Station A	Station G	Station C	All Data	Cosmogenic ν's
Triggers	203562	248772	512931	965265	100%
$\alpha < -0.45$	51327 (25%)	102599 (41%)	142243 (28%)	296169 (31%)	99.5%
$\eta > 3$	3159 (2%)	26868 (11%)	13461 (3%)	43488 (4.5%)	97%
$\chi > 0.81$	0 (0%)	0 (0%)	0 (0%)	0 (0%)	90%

Table 2: A summary of the number of neutrino candidates remaining with the successive application of each cut. The fractions in parentheses are with respect to the totals. See text for a brief discussion of the excess background in the data from Station G.

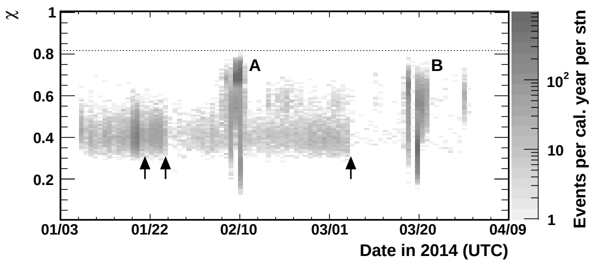

Figure 20: The χ value of events with $\alpha < -0.45$ and $\eta > 3$ on all three stations is shown as a function of time. A sharp reduction in pure thermal events is seen after threshold tunings, indicated by the arrows (each station was tuned only twice, but not all on the same days). An excess of non-thermal background events is seen during the high wind periods indicated by "A" and "B." The dotted line indicates the neutrino candidate cut ($\chi > 0.81$) applied in the analysis.

data around $\chi \approx 0.68$, visible in Fig. 19.

The application of all cuts preserves 90% of the cosmogenic neutrino triggers while removing all events recorded by the HRA-3 during the 2013-14 data taking season. A summary of the number of neutrino candidates that remain after the successive application of each selection criterion is presented in Table 2.

The analysis of the 2013-14 HRA-3 data has employed a similar procedure to that used on the HRA-3 data from the 2012-13 season [82] and on prototype HRA-1 data [84]. These analyses also found high signal efficiency values using background rejection procedures that produced no neutrino candidate events.

4.3. Flux Limit

An upper limit on the total diffuse neutrino flux can be determined due to the absence of any observed events. With no observed events and no background events, the Neyman formalism is used to place an upper limit of 2.3 neutrino events at the 90% confidence level in each energy bin. Figure 21

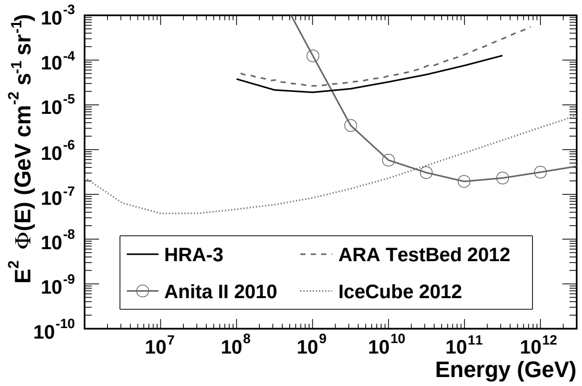

Figure 21: The 90% confidence level Neyman upper limit on the all flavor $\nu + \bar{\nu}$ flux, calculated in a sliding decade-wide energy bin, arising from the lack of neutrino candidate events in the HRA-3 data set collected during the 2013-14 season. The limit is compared to that of the ARA TestBed [25] as well as to the current best limits set by Anita II [15, 16] at high energies and IceCube [12] at lower energies.

shows this limit translated to a limit on the all flavor neutrino flux as a function of neutrino energy. No neutrino flux model has been assumed in the calculation of the limit. Instead, Eq. 1 is used to determine the flux that would produce 2.3 neutrinos in a sliding decade-wide energy bin by taking E to be the energy at the center of the bin, $dN \leq 2.3$ to be the limit on the number of neutrinos in the energy bin and $dE = E \ln 10 d\log E = E \ln 10$ to be the width of the decade-wide energy bin. That is,

$$E^2\Phi(E) \leq \frac{2.3\ E}{\ln 10} \frac{L(E)}{\varepsilon V_{eff} \Omega\ t_{live}} \quad (2)$$

where $V_{eff}\Omega$ is the single station effective volume, averaged over neutrino flavor, shown in Fig. 4. Also shown in Fig. 21 is the recent limit placed by the ARA TestBed detector with 224 days of livetime [25], as well as the current best limits from Anita II [15, 16] at high energies and IceCube [12] at lower energies. Decade-wide energy bins have been chosen to facilitate comparison with the differential limits from ARA and IceCube.

4.4. The Full ARIANNA Detector

A search for neutrino signals in the data from the full ARIANNA detector will make use of all information recorded by the detector in each event. Full likelihood fits will be used to reconstruct the radio signal direction, the incoming neutrino direction and the neutrino energy. This will facilitate the use of further, and almost certainly more powerful, selection criteria with which to separate neutrino signals from radio backgrounds.

However, it is worthwhile to investigate how the simple analysis presented in this article would perform for data taken by the full detector. For this purpose, the full detector is taken to operate for 58% of the year, from mid-September to early April, and to consist of 1296 stations.

The deadtime of the full detector will be reduced relative to that of the HRA-3 stations. With the autocorrelation filter implemented as a local level zero trigger (see Sect. 4.2) average event rates of 10^{-4} Hz are easily achievable, even with 4σ thresholds. Each station can then immediately send every event off site via the Iridium SBD satellite connection, allowing near real-time data transfer. With such a setup, each station would transfer fewer than 9 events per day, leading to a deadtime of 2% due to data transfer and communications. The calibration data will likely be collected somewhat less often, leading to a deadtime of $< 1\%$.

Figure 22 shows the cumulative number of background events expected to pass a $\chi > C$ cut as a function of the cut value, C. The cumulative distribution is obtained by scaling that of the HRA-3 analysis (see Fig. 19) up to the livetime expected for a 1296 station detector running for 58% of 3 years. An exponential function is fit to the tail of the cumulative distribution in order to determine the correlation cut necessary to admit only 0.3 background events in the full detector data set. The extrapolated correlation cut value of $\chi > 0.87$ preserves 83% of the cosmogenic neutrino triggers. This result assumes, by necessity, that no new type of background event will be observed that changes the shape of the tail of the correlation cut distribution.

The signal efficiency for an analysis with the full ARIANNA detector should further improve, given the expectation that a reconstruction of the neutrino angle and energy will strengthen the signal

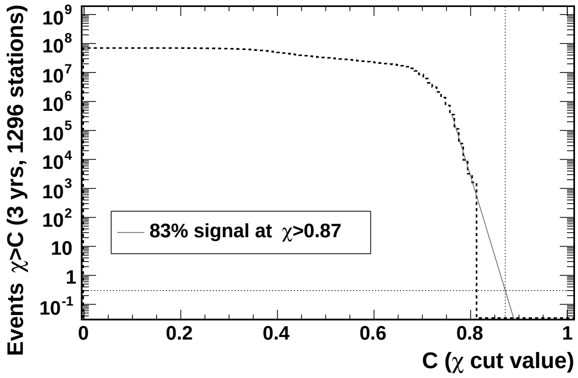

Figure 22: The cumulative background distribution from the current HRA-3 analysis, scaled up to a livetime equivalent to 1296 stations running for 58% of 3 years. The solid grey line shows an exponential fit to the tail used to extrapolate the cut necessary to allow 0.3 background events in the full detector data set. This cut preserves 83% of the cosmogenic neutrino triggers.

and background separation. Also note that the extrapolation of the HRA-3 data includes background events caused by cosmic rays. The prior rejection of cosmic rays using upward facing antennas, as described in Sect. 2.3, may reduce the background further, allowing for a less strict χ cut and a correspondingly improved signal efficiency.

5. Conclusions

The ARIANNA experiment proposes the use of the Askaryan effect to search for a diffuse flux of neutrinos in the $10^8 - 10^{10}$ GeV energy range. The experiment will exploit the long attenuation length of ice at radio frequencies by populating the surface of the Ross Ice Shelf of Antarctica with a grid of radio detectors to reach an effective volume on the order of 100 km^3. The ice to water interface at the bottom of the ice shelf acts as a mirror to radio pulses, making ARIANNA sensitive to neutrinos arriving from above the detector as well as from the horizon.

The response of such a detector to the electric fields generated by the Askaryan effect has been simulated in both the frequency and time domains. The angular resolution of the neutrino direction is found to be about 2.9° in the local zenith angle and 2.5° in the local azimuth angle. Determination of the angle between the Cherenkov cone peak and the observation angle of the detector to within 1.5°

improves the angular resolution on the neutrino direction by 50% in zenith and 20% in azimuth. The resolution on the energy of the neutrino is found to be about a factor of 5 with no knowledge of the Cherenkov observation angle, and a factor of 2.2 if the angle is known to about 1.4° on average.

To facilitate the construction of the full ARIANNA detector, a prototype of seven radio detector stations, the HRA, is currently under construction at the Ross Ice Shelf. During the 2013-14 austral summer, three such stations collected radio data. This data set has been analyzed in a search for high energy neutrino signals. No neutrino-like signals were found in the data. The majority of data collected consists of purely random thermal triggers. Two other principal sources of backgrounds were observed, one showing oscillatory waveforms indicative of detector electronics effects and another associated with periods of high winds at the site.

The rejection of these backgrounds by a simple analysis that does not rely on reconstructing the radio signal direction is found to preserve 90% of cosmogenic neutrino triggers. A model-independent differential upper limit has been placed at the 90% confidence level on the all flavor $\nu + \bar{\nu}$ flux in a sliding decade-wide energy bin. The limit reaches a minimum of $1.9{\times}10^{-23}$ GeV^{-1} cm^{-2} s^{-1} sr^{-1} in the $10^{8.5} - 10^{9.5}$ GeV energy bin.

The analysis presented in this article has been extrapolated to the full 1296 station ARIANNA experiment being run during the austral summer for 3 years. Background rejection levels are found that allow only 0.1 background events per year in the entire detector while preserving 83% of cosmogenic neutrino triggers. The actual performance of the full experiment may be further improved by the reconstruction of the neutrino direction and energy.

The ARIANNA experiment has the potential to extend the measurement of the diffuse neutrino flux to higher neutrino energies by two orders of magnitude in energy. The current UHE neutrino flux measurement by the IceCube collaboration [61] would produce about 2.8 neutrinos in 3 calendar years of ARIANNA data, even if there is no additional source of high energy neutrinos, as shown in Table 1. A measurement of the neutrino flux at such energies would likely generate comparable levels of interest in the growing field of ultra-high energy neutrino astronomy. Measurements of the diffuse flux could be improved by expanding the array, while dedicated point searches with improved angular resolution could be performed by increasing the density of the array.

6. Acknowledgements

The authors wish to thank the staff of Antarctic Support Contractors, Lockheed, and the entire crew at McMurdo Station for excellent logistical support. The authors also thank Prof. De Flaviis for the use of the Far Field Anechoic Chamber at U.C. Irvine and would like to acknowledge and thank the CReSIS project and the Anechoic Chamber facility management for the use of the world class anechoic chamber at the University of Kansas.

This work was supported by generous funding from the Office of Polar Programs and the Physics Division of the US National Science Foundation, including via grant awards ANT-08339133, NSF-0970175, and NSF-1126672.

References

[1] A. Letessier-Selvon, T. Stanev, Ultrahigh Energy Cosmic Rays, Rev.Mod.Phys. 83 (2011) 907–942. arXiv:1103.0031, doi:10.1103/RevModPhys.83.907.

[2] P. Abreu, et al., Constraints on the origin of cosmic rays above 10^{18} eV from large scale anisotropy searches in data of the Pierre Auger Observatory, Astrophys.J. 762 (2012) L13. arXiv:1212.3083, doi:10.1088/2041-8205/762/1/L13.

[3] T. J. Weiler, Extreme energy cosmic rays: Puzzles, models, and maybe neutrinos, AIP Conf.Proc. 579 (2001) 58–77. arXiv:hep-ph/0103023, doi:10.1063/1.1398161.

[4] G. Sigl, The Enigma of the highest energy particles of nature, Annals Phys. 303 (2003) 117–141. arXiv:astro-ph/0210049, doi:10.1016/S0003-4916(02)00021-0.

[5] G. Sigl, Particle and astrophysics aspects of ultrahigh-energy cosmic rays, Lect.Notes Phys. 556 (2000) 259–300. arXiv:astro-ph/0008364.

[6] K. Greisen, End to the cosmic ray spectrum?, Phys.Rev.Lett. 16 (1966) 748–750. doi:10.1103/PhysRevLett.16.748.

[7] G. Zatsepin, V. Kuzmin, Upper limit of the spectrum of cosmic rays, JETP Lett. 4 (1966) 78–80.

[8] F. Stecker, Ultrahigh energy photons, electrons and neutrinos, the microwave background, and the universal cosmic ray hypothesis, Astrophys.Space Sci. 20 (1973) 47–57. doi:10.1007/BF00645585.

[9] V. Berezinsky, G. Zatsepin, Cosmic rays at ultrahigh-energies (neutrino?), Phys.Lett. B28 (1969) 423–424. doi:10.1016/0370-2693(69)90341-4.

[10] V. Berezinsky, A. Y. Smirnov, Cosmic neutrinos of ultra-high energies and detection possibility, Astrophys.Space Sci. 32 (1975) 461–482. doi:10.1007/BF00643157.

[11] J. Ahrens, et al., Search for extraterrestrial point sources of neutrinos with AMANDA-II, Phys.Rev.Lett. 92 (2004) 071102. arXiv:astro-ph/0309585, doi:10.1103/PhysRevLett.92.071102.

[12] M. Aartsen, et al., Probing the origin of cosmic-rays with extremely high energy neutrinos using the IceCube Observatory, Phys.Rev. D88 (2013) 112008. arXiv:1310.5477.

[13] F. Halzen, S. R. Klein, IceCube: An Instrument for Neutrino Astronomy, Rev.Sci.Instrum. 81 (2010) 081101. arXiv:1007.1247, doi:10.1063/1.3480478.

[14] P. Gorham, et al., New Limits on the Ultra-high Energy Cosmic Neutrino Flux from the ANITA Experiment, Phys.Rev.Lett. 103 (2009) 051103. arXiv:0812.2715, doi:10.1103/PhysRevLett.103.051103.

[15] P. Gorham, et al., Observational constraints on the ultrahigh energy cosmic neutrino flux from the second flight of the anita experiment, Phys. Rev. D 82 (2010) 022004. doi:10.1103/PhysRevD.82.022004.

[16] P. Gorham, et al., Erratum: Observational Constraints on the Ultra-high Energy Cosmic Neutrino Flux from the Second Flight of the ANITA Experiment, Phys.Rev. D85 (2012) 049901. arXiv:1011.5004, doi:10.1103/PhysRevD.82.022004,10.1103/PhysRevD.85.049901.

[17] I. Kravchenko, et al., Limits on the ultra-high energy electron neutrino flux from the RICE experiment, Astropart.Phys. 20 (2003) 195–213. arXiv:astro-ph/0206371, doi:10.1016/S0927-6505(03)00181-6.

[18] I. Kravchenko, et al., Rice limits on the diffuse ultrahigh energy neutrino flux, Phys.Rev. D73 (2006) 082002. arXiv:astro-ph/0601148, doi:10.1103/PhysRevD.73.082002.

[19] J. Abraham, et al., Upper limit on the diffuse flux of UHE tau neutrinos from the Pierre Auger Observatory, Phys.Rev.Lett. 100 (2008) 211101. arXiv:0712.1909, doi:10.1103/PhysRevLett.100.211101.

[20] J. Abraham, et al., Limit on the diffuse flux of ultra-high energy tau neutrinos with the surface detector of the Pierre Auger Observatory, Phys.Rev. D79 (2009) 102001. arXiv:0903.3385, doi:10.1103/PhysRevD.79.102001.

[21] R. U. Abbasi, et al., An upper limit on the electron-neutrino flux from the HiRes detector, Astrophys.J. 684 (2008) 790–793. arXiv:0803.0554, doi:10.1086/590335.

[22] K. Martens, Hires estimates and limits for neutrino fluxes at the highest energies (2007). arXiv:0707.4417.

[23] M. Aartsen, et al., Observation of High-Energy Astrophysical Neutrinos in Three Years of IceCube Data, Phys.Rev.Lett. 113 (2014) 101101. arXiv:1405.5303, doi:10.1103/PhysRevLett.113.101101.

[24] P. Allison, et al., Design and Initial Performance of the Askaryan Radio Array Prototype EeV Neutrino Detector at the South Pole, Astropart.Phys. 35 (2012) 457–477. arXiv:1105.2854, doi:10.1016/j.astropartphys.2011.11.010.

[25] P. Allison, et al., First Constraints on the Ultra-High Energy Neutrino Flux from a Prototype Station of the Askaryan Radio Array, Submitted to Astropart.Phys.arXiv:1404.5285.

[26] A. G. Vieregg, D. Saltzberg, Greenland Neutrino Observatory(GNO): Radio Detector of Ultra-high Energy Neutrinos at Apex Station in Greenland (2014).
URL http://kicp.uchicago.edu/~avieregg/gnoWhitepaper.pdf

[27] P. W. Gorham, Particle Astrophysics in NASA's Long Duration Balloon Program, Nucl.Phys.Proc.Suppl. 243-244 (2013) 231–238. doi:10.1016/j.nuclphysbps.2013.09.012.

[28] P. Gorham, F. Baginski, P. Allison, K. Liewer, C. Miki, et al., The ExaVolt Antenna: A Large-Aperture, Balloon-embedded Antenna for Ultra-high Energy Particle Detection, Astropart.Phys. 35 (2011) 242–256. arXiv:1102.3883, doi:10.1016/j.astropartphys.2011.08.004.

[29] G. A. Askaryan, JETP 14 (1962) 441.

[30] G. A. Askaryan, JETP 21 (1965) 658.

[31] D. Saltzberg, P. Gorham, D. Walz, et al., Observation of the Askaryan effect: Coherent microwave Cherenkov emission from charge asymmetry in high-energy particle cascades, Phys.Rev.Lett. 86 (2001) 2802–2805. arXiv:hep-ex/0011001, doi:10.1103/PhysRevLett.86.2802.

[32] P. Gorham, et al., Observations of the Askaryan effect in ice, Phys.Rev.Lett. 99 (2007) 171101. arXiv:hep-ex/0611008, doi:10.1103/PhysRevLett.99.171101.

[33] J. Alvarez-Muniz, R. Vazquez, E. Zas, Calculation methods for radio pulses from high-energy showers, Phys.Rev. D62 (2000) 063001. arXiv:astro-ph/0003315, doi:10.1103/PhysRevD.62.063001.

[34] S. W. Barwick, et al., Radio-frequency attenuation length, basal reflectivity, depth, and polarization measurements from moores bay in the ross ice-shelf, Accepted for publication in J.Glaciol.

[35] J. A. Dowdeswell, S. Evans, Investigations of the form and flow of ice sheets and glaciers using radio-echo sounding, Reports on Progress in Physics 67 (10) (2004) 1821.
URL http://stacks.iop.org/0034-4885/67/i=10/a=R03

[36] S. W. Barwick for the ARIANNA Collaboration, Performance of the ARIANNA Prototype Array, in: Proc. 33rd Intern. Cosmic Ray Conf., 2013.

[37] K.-H. Kampert, M. Unger, Measurements of the Cosmic Ray Composition with Air Shower Experiments, Astropart.Phys. 35 (2012) 660–678. arXiv:1201.0018, doi:10.1016/j.astropartphys.2012.02.004.

[38] R. Engel, D. Seckel, T. Stanev, Neutrinos from propagation of ultrahigh-energy protons, Phys.Rev. D64 (2001) 093010. arXiv:astro-ph/0101216, doi:10.1103/PhysRevD.64.093010.

[39] D. Seckel, T. Stanev, Neutrinos: The Key to UHE cosmic rays, Phys.Rev.Lett. 95 (2005) 141101. arXiv:astro-ph/0502244, doi:10.1103/PhysRevLett.95.141101.

[40] A. Connolly, R. S. Thorne, D. Waters, Calculation of High Energy Neutrino-Nucleon Cross Sections and Uncertainties Using the MSTW Parton Distribution Functions and Implications for Future Experiments, Phys.Rev. D83 (2011) 113009. arXiv:1102.0691, doi:10.1103/PhysRevD.83.113009.

[41] S. R. Klein, A. Connolly, Neutrino Absorption in the Earth, Neutrino Cross-Sections, and New PhysicsarXiv:1304.4891.

[42] S.-H. Wang, P. Chen, M. Huang, J. Nam, Feasibility of Determining Diffuse Ultra-High Energy Cosmic Neutrino Flavor Ratio through ARA Neutrino Observatory, JCAP 1311 (2013) 062. arXiv:1302.1586, doi:10.1088/1475-7516/2013/11/062.

[43] A. V. Olinto, K. Kotera, D. Allard, Ultrahigh Energy Cosmic Rays and Neutrinos, Nucl.Phys.Proc.Suppl. 217 (2011) 231–236. arXiv:1102.5133, doi:10.1016/j.nuclphysbps.2011.04.109.

[44] K. Dookayka, Characterizing the Search for Ultra-High Energy Neutrinos with the ARIANNA Detector, Ph.D.

thesis, University of Californa, Irvine (2011).
[45] F. Halzen, D. Saltzberg, Tau-neutrino appearance with a 1000 megaparsec baseline, Phys.Rev.Lett. 81 (1998) 4305–4308. arXiv:hep-ph/9804354, doi:10.1103/PhysRevLett.81.4305.
[46] R. Gandhi, C. Quigg, M. H. Reno, I. Sarcevic, Neutrino interactions at ultrahigh-energies, Phys.Rev. D58 (1998) 093009. arXiv:hep-ph/9807264, doi:10.1103/PhysRevD.58.093009.
[47] T. K. Gaisser, F. Halzen, T. Stanev, Particle astrophysics with high-energy neutrinos, Phys.Rept. 258 (1995) 173–236. arXiv:hep-ph/9410384, doi:10.1016/0370-1573(95)00003-Y.
[48] R. Gandhi, C. Quigg, M. H. Reno, I. Sarcevic, Ultrahigh-energy neutrino interactions, Astropart.Phys. 5 (1996) 81–110. arXiv:hep-ph/9512364, doi:10.1016/0927-6505(96)00008-4.
[49] J. Alvarez-Muniz, E. Zas, The LPM effect for EeV hadronic showers in ice: Implications for radio detection of neutrinos, Phys.Lett. B434 (1998) 396–406. arXiv:astro-ph/9806098, doi:10.1016/S0370-2693(98)00905-8.
[50] J. Alvarez-Muniz, E. Zas, Cherenkov radio pulses from Eev neutrino interactions: The LPM effect, Phys.Lett. B411 (1997) 218–224. arXiv:astro-ph/9706064, doi:10.1016/S0370-2693(97)01009-5.
[51] L. Gerhardt, S. R. Klein, Electron and Photon Interactions in the Regime of Strong LPM Suppression, Phys.Rev. D82 (2010) 074017. arXiv:1007.0039, doi:10.1103/PhysRevD.82.074017.
[52] C. B. V. Bogorodsky, P. E. Gudmandsen, Radioglaciology, Reidel Publishing Co. (The Netherlands), 1985.
[53] V. Schytt, Scientific results, Norsk Polarinstitutt (Norwegian-British-Swedish Antarctic Expedition) (1958) 113–151.
[54] T. Barrella, S. W. Barwick, D. Saltzberg, Ross Ice Shelf in situ radio-frequency ice attenuation, J.Glaciol. 57 (2011) 61–66. arXiv:1011.0477, doi:10.3189/002214311795306691.
[55] S. Barwick, E. Berg, D. Besson, T. Duffin, J. Hanson, et al., Time Domain Response of the ARIANNA Detector, Astropart.Phys. 62 (2014) 139–151. arXiv:1406.0820, doi:10.1016/j.astropartphys.2014.09.002.
[56] J. Alvarez-Muniz, A. Romero-Wolf, E. Zas, Cherenkov radio pulses from electromagnetic showers in the time-domain, Phys.Rev. D81 (2010) 123009. arXiv:1002.3873, doi:10.1103/PhysRevD.81.123009.
[57] J. Alvarez-Muniz, A. Romero-Wolf, E. Zas, Practical and accurate calculations of Askaryan radiation, Phys.Rev. D84 (2011) 103003. arXiv:1106.6283, doi:10.1103/PhysRevD.84.103003.
[58] P. Abreu, et al., Search for point-like sources of ultra-high energy neutrinos at the Pierre Auger Observatory and improved limit on the diffuse flux of tau neutrinos, Astrophys.J. 755 (2012) L4. arXiv:1210.3143, doi:10.1088/2041-8205/755/1/L4.
[59] R. Abbasi, et al., Constraints on the Extremely-high Energy Cosmic Neutrino Flux with the IceCube 2008-2009 Data, Phys.Rev. D83 (2011) 092003. arXiv:1103.4250, doi:10.1103/PhysRevD.84.079902, 10.1103/PhysRevD.83.092003.
[60] I. Kravchenko, S. Hussain, D. Seckel, D. Besson, E. Fensholt, et al., Updated Results from the RICE Experiment and Future Prospects for Ultra-High Energy Neutrino Detection at the South Pole, Phys.Rev. D85 (2012) 062004. arXiv:1106.1164, doi:10.1103/PhysRevD.85.062004.
[61] M. Aartsen, et al., Evidence for High-Energy Extraterrestrial Neutrinos at the IceCube Detector, Science 342 (2013) 1242856. arXiv:1311.5238, doi:10.1126/science.1242856.
[62] E. Waxman, J. N. Bahcall, High-energy neutrinos from astrophysical sources: An Upper bound, Phys.Rev. D59 (1999) 023002. arXiv:hep-ph/9807282, doi:10.1103/PhysRevD.59.023002.
[63] H. Yuksel, M. D. Kistler, Enhanced cosmological GRB rates and implications for cosmogenic neutrinos, Phys.Rev. D75 (2007) 083004. arXiv:astro-ph/0610481, doi:10.1103/PhysRevD.75.083004.
[64] K. Kotera, D. Allard, A. V. Olinto, Cosmogenic Neutrinos: parameter space and detectability from PeV to ZeV, JCAP 1010 (2010) 013. arXiv:1009.1382, doi:10.1088/1475-7516/2010/10/013.
[65] S. Yoshida, M. Teshima, Energy spectrum of ultrahigh-energy cosmic rays with extragalactic origin, Prog.Theor.Phys. 89 (1993) 833–845. doi:10.1143/PTP.89.833.
[66] M. Ahlers, L. Anchordoqui, M. Gonzalez-Garcia, F. Halzen, S. Sarkar, GZK Neutrinos after the Fermi-LAT Diffuse Photon Flux Measurement, Astropart.Phys. 34 (2010) 106–115. arXiv:1005.2620, doi:10.1016/j.astropartphys.2010.06.003.
[67] M. Ave, N. Busca, A. V. Olinto, A. A. Watson, T. Yamamoto, Cosmogenic neutrinos from ultra-high energy nuclei, Astropart.Phys. 23 (2005) 19–29. arXiv:astro-ph/0409316, doi:10.1016/j.astropartphys.2004.11.001.
[68] K. Fang, K. Kotera, K. Murase, A. V. Olinto, A decisive test for the young pulsar origin of ultrahigh energy cosmic rays with IceCube. arXiv:1311.2044.
[69] S. W. Barwick, et al., Design and Performance of the ARIANNA Hexagonal Radio Array Systems, Submitted to IEEE Trans.Nucl.Sci.
[70] C. Reed, for the ARIANNA Collaboration, Performance of the ARIANNA Neutrino Telescope Stations, in: Proc. 33rd Intern. Cosmic Ray Conf., 2013.
[71] T. Huege, M. Ludwig, C. W. James, Simulating radio emission from air showers with CoREASarXiv:1301.2132.
[72] T. Huege, The Renaissance of Radio Detection of Cosmic Rays, in: Proc. 33rd Intern. Cosmic Ray Conf., 2013, highlight Contribution. arXiv:1310.6927.
[73] T. Huege, C. W. James, Full Monte Carlo simulations of radio emission from extensive air showers with CoREAS. arXiv:1307.7566.
[74] D. Heck, G. Schatz, T. Thouw, J. Knapp, J. Capdevielle, CORSIKA: A Monte Carlo code to simulate extensive air showers.
[75] S. Ostapchenko, Non-linear screening effects in high energy hadronic interactions, Phys.Rev. D74 (2006) 014026. arXiv:hep-ph/0505259, doi:10.1103/PhysRevD.74.014026.
[76] P. Abreu, et al., The Pierre Auger Observatory I: The Cosmic Ray Energy Spectrum and Related Measurements. arXiv:1107.4809.
[77] Gerhardt, Lisa and others, A prototype station for ARIANNA: a detector for cosmic neutrinos, Nucl.Instrum.Meth. A624 (2010) 85–91. arXiv:1005.5193, doi:10.1016/j.nima.2010.09.032.
[78] S. Kleinfelder for the ARIANNA Collaboration, Design

and performance of the autonomous data acquisition system for the arianna high energy neutrino detector, Nuclear Science, IEEE Transactions on 60 (2) (2013) 612–618. doi:10.1109/TNS.2013.2252365.

[79] S. Kleinfelder, S. Chiang, W. Huang, Multi-GHz synchronous waveform acquisition with real-time pattern-matching trigger generation, Nuclear Science, IEEE Transactions on 60 (5) (2013) 3785–3792. doi:10.1109/TNS.2013.2279660.

[80] Model AR-24027E, AFAR Communications Inc., Santa Barbara, CA (2008).

[81] Model 9602-N, NAL Research Corp., Manassas, VA (2010).

[82] J. E. Tatar, Performance of Sub-Array of ARIANNA Detector Stations during First Year of Operation, Ph.D. thesis, University of Californa, Irvine (2013).

[83] G. Upton, I. Cook, A Dictionary of Statistics, 2nd Edition, Oxford University Press, 2008.

[84] J. C. Hanson, The Performance and Initial Results of the ARIANNA Prototype, Ph.D. thesis, University of Californa, Irvine (2013).